

## Original article

# Study on the seismic damage and dynamic support of roadway surrounding rock based on reconstructive transverse and longitudinal waves

Shengquan He<sup>1,2,3</sup>, Feng Shen<sup>1,3</sup>, Tuo Chen<sup>2</sup>\*, Hani Mitri<sup>2</sup>, Ting Ren<sup>4</sup>, Dazhao Song<sup>1,3</sup>

<sup>1</sup>Key Laboratory of Ministry of Education for Efficient Mining and Safety of Metal Mine, University of Science and Technology Beijing, Beijing 100083, P. R. China

<sup>2</sup>Department of Mining and Materials Engineering, McGill University, Montreal, H3A 0E8, Canada

<sup>3</sup>Research Institute of Macro-Safety Science, University of Science and Technology Beijing, Beijing 100083, P. R. China

<sup>4</sup>School of Civil, Mining and Environmental Engineering, University of Wollongong, Wollongong, NSW 2522, Australia

### Keywords:

Seismic event  
dynamic simulation  
wave decomposition  
response characteristics  
roadway support

### Cited as:

He, S., Shen, F., Chen, T., Mitri, H., Ren, T., Song, D. Study on the seismic damage and dynamic support of roadway surrounding rock based on reconstructive transverse and longitudinal waves. *Advances in Geo-Energy Research*, 2023, 9(3): 156-171.  
<https://doi.org/10.46690/ager.2023.09.04>

### Abstract:

The magnitude and frequency of induced seismicity increase as mining excavation reaches greater depth, leading to the increasingly severe damage to roadways caused by high-energy seismic waves. To comprehensively simulate the damage caused by dynamic loads, a synchrosqueezing transform and empirical mode decomposition method was developed, which effectively decomposed raw seismic wave signals into transverse and longitudinal components. This novel method produced more accurate results in terms of velocity, displacement, rock yielding patterns, and reflecting theoretically orthogonal oscillating directions of transverse and longitudinal waves compared to using raw mixed waves at the seismic source. Under the disturbance of transverse and longitudinal waves, the vertical displacement was much higher than horizontal displacement at the top position of the roadway, while the horizontal displacement was greater at the sidewalls. The particle vibration velocity, displacement and yielding zone of the surrounding rock of roadway were proportional to the energy level of seismic, while inversely proportional to the source-roadway distance. The proportion of damage attributed to transverse waves increased with the energy level, ranging from 75.8% to 85.8%. Eventually, a roadway dynamic support design was optimized based on the proposed seismic wave processing and modeling methodology. The methodology offers guidance for roadway dynamic support design, with the goal of averting excessive or insufficient support strength.

## 1. Introduction

As one of the primary energy sources globally, the mining of coal seams is inevitably going deeper due to the gradual depletion of shallow coal resources. This shift is crucial for ensuring the energy security of countries with limited access to oil and gas (Ranjith et al., 2017; Chu et al., 2023a, 2023b). With increasing mining depth, the energy level and frequency of mining-induced seismic events are rising, resulting in more severe deformation and damage of roadways underground (Tan et al., 2019; Sabagh and Ghalandarzadeh, 2020; Hossein-

zadehsabeti et al., 2021). The dynamic loads leading to the deformation and damage of the roadway mainly come from the large-magnitude seismic events generated by the slip of geological structures under high stress. At present, mining-induced seismicity is mainly monitored by microseismic monitoring systems that record seismic waves through subsurface geophones and accelerometers in real time.

The influence of dynamic loads on rock mass damage and roadway support has been studied extensively by researchers. Mishra et al. (2022) suggested that the subsidence in roadway under dynamic loads are basically the function

of impact energies, characteristics of surrounding rock mass, depth and induced stresses. Zhou et al. (2022) quantified the mechanical response characteristics of rock masses to dynamic loads by single and cyclic impact compression tests using a split hopkinson pressure bar apparatus. Dhamne et al. (2021) found that the depth of the covering layer plays a crucial role in determining overall stress and deformation when the roadway is subjected to dynamic loads. Mishra et al. (2021) analyzed the damage pattern of the roadway under blast loads using a combination of numerical simulation and experimental methods. Kim et al. (2021) investigated the progressive damage evolution of in-situ rock under dynamic loading conditions by acoustic emission monitoring. Mitelman and Elmo (2016) pointed out that when blast stress waves are transmitted to the roadway boundary, they will reflect and convert into tensile stress waves, leading to roadway damage. Zuo et al. (2022) showed that the absorbed energy per unit volume and the crushing energy per unit mass of rock are closely related to the dynamic compressive strength of split hopkinson pressure bar. As the incident energy increases, the crushing energy of the rock increases and the energy dissipation intensifies. Meanwhile, some scholars have studied the impacts of rock tensile strength and the magnitude of incident seismic waves on the roadway damage (Schuler et al., 2006; Lamur et al., 2023). The stress distribution in the roadway surrounding rock varies greatly in different areas under the incident disturbance of seismic wave, and the tensile stress induced by the incident seismic wave is an important cause of roadway damage (Fan et al., 2019; Feng et al., 2020; Ghaychi Afrouz et al., 2022). Since it is challenging to reflect the real-time stress response of the surrounding rock empirically, numerical research has been conducted on the dynamic stress field of roadway during dynamic loading. The effect of dynamic loading on the rock damage can be modelled by solving dynamic equations. (Emad et al., 2018; Shi et al., 2021). Wicaksana et al. (2021) explored the problem of mechanical cutting of rock masses through dynamic finite-element modeling. Their findings indicated that simulations incorporating dynamic inputs more accurately mirrored laboratory results with reduced deviations. Wang et al. (2022) employed Fast Lagrangian Analysis of Continua in Three-dimensions (FLAC3D) modeling code to elaborate the stability of roadway roof under multiple dynamic load perturbations. It showed that the roadway was subjected to greater damage under the effect of dynamic and static superposition. He et al. (2020) used FLAC3D to back analyze rockburst events triggered by a remote seismic source. The outcomes revealed that seismic waves damaged a large span of roadways ahead of the working face, consistent with the field observation.

Scholars have extensively studied the stability characteristics of the roadway under various support systems. Basarir et al. (2019) proposed a support system consisting of rock bolt, cable bolt and shotcrete in order to cope with the displacements caused by large-scale mining operations, resulting in a considerable reduction rock displacements. Zang et al. (2021) proposed an integrated support scheme of “double anchor cable + wire mesh + W steel belt”, which improved the bearing capacity of the surrounding rock effectively. Sakhno

and Sakhno (2023) investigated the dynamic stress and strain distribution in the surrounding rock by numerical simulation. They recommended grouting reinforcement to control the floor bulge. Forbes et al. (2020), identified a close correlation between the effectiveness of perimeter rock anchoring and the mechanical properties of the support components through in-situ tension tests on the support elements. Ghorbani et al. (2020) emphasized the importance of designing a support system capable of absorbing both the kinetic energy radiated by seismic events and the potential energy associated with falling rock blocks during dynamic conditions. However, effectively supporting the roadway under complex dynamic loading conditions remains a formidable challenge (Perazzellin and Anagnostou, 2013; Rodríguez and Díaz-Aguado, 2013; Li et al., 2020a).

The natural seismic waves generated during coal and rock fracturing are mixed and mainly composed of P (longitudinal) and S (transverse) waves. The present coal mine microseismic monitoring systems collect mixed seismic waves without distinguishing P and S waves. The P and S waves displacement fields are shown in Fig. 1, indicating significant differences in their damage effects when passing through a medium (Feng et al., 2016). To reveal the mechanism of seismic wave on coal rock and realize seismic wave decomposition, scholars worldwide have undertaken valuable research. Herrera et al. (2014) extracted the longitudinal waves by intercepting a fixed-length waveform backward with the initial starting point, but the subsequent P wave mixed in the S wave part were not separated out. Wang et al. (2002) proposed a method for decomposing the P and S wave fields from multicomponent seismic data based on the linear transformation. Li et al. (2013) and De Lauro et al. (2016) proposed multicomponent wave separation methods using the equivalent elastic fluctuation equation and independent component analysis. To date, there is still an absence of mature techniques for decomposing the mixed parts of P and S waves. Consequently, numerous modeling studies have limited their analysis of the seismic damage characteristics of roadway to the application of mixed seismic waveforms, often overlooking the complexity of seismic wave signals and the distinctions between P and S waves in terms of oscillation directions (Fig. 1).

To address the abovementioned issue, this study developed a seismic wave decomposition and reconstruction method based on synchrosqueezing transform and empirical mode decomposition (SST-EMD). The damage characteristics of roadway surrounding rocks under different microseismic energy, source-roadway distance and different seismic wave application methods were comprehensively studied through dynamic modeling. Ultimately, a targeted dynamic support scheme based on the modeling results was proposed.

## 2. SST-EMD decomposition of mixed seismic wave

The SST algorithm is a time-frequency domain rearrangement algorithm developed based on wavelet transform, which not only has high time-frequency resolution, but also offers support for signal reconstruction. As a result, it enables the

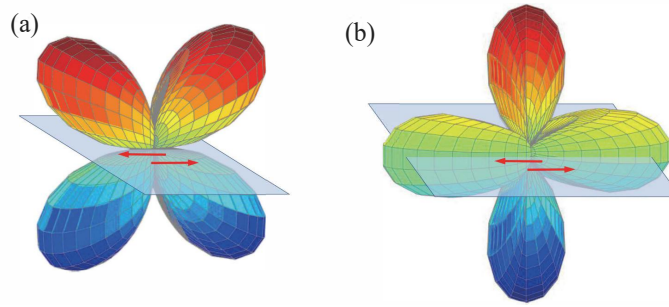


**Fig. 1.** Spatial distribution of P and S wave displacement fields due to a shear fracture (red arrows are located at the fracture surface). (a) P wave and (b) S wave.

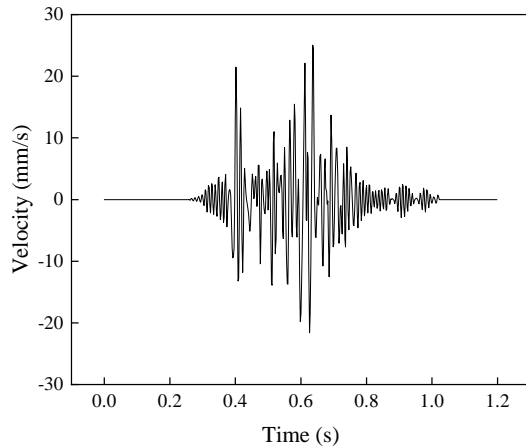


**Fig. 2.** In-situ original waveform monitoring results.

identification of P and S waves with broad ranges of frequencies within the time-frequency spectrum, which can accurately extract the arrival time of S wave. During wave reconstruction, the method also supports the removal of noises on the time-frequency map. More details of the SST method can be found in the published paper of the previous study (He et al., 2020). Fig. 2 shows a raw time-velocity waveform from a seismic event of  $10^7$  J received by the microseismic monitoring system of the Wudong Coal Mine, China.

After applying SST, the P and S waves effective signals with different frequency components were visualized in the time-frequency spectrum (Fig. 3). The figure indicates the accurate arrival time of S wave. Fig. 4 shows the reconstruction results of the P wave signal before the arrival of the S wave, and P/S mixed wave (S wave mixed with the tail of P wave). This approach lays a strong foundation for the subsequent mixed waveform decomposition.

The previous research showed a preliminary trial to decompose mixed seismic waveform (He et al., 2020). Although S wave arrival can be identified correctly using SST method, there is still P/S mixed wave that was not separated after the arrival of the S wave. To further achieve the fully decomposition of P and S waves, the SST-EMD method was proposed in this study. The empirical modal decomposition (EMD) method is an adaptive signal decomposition method that applies a nonlinear filtering operator to transform a non-smooth, nonlinearly varying signal, e.g., raw seismic signals, into a finite

number of intrinsic mode functions (IMFs) with only single-frequency components at any moment, independent of the selection of the basic functions. EMD has been widely used in biomedicine, mechanical equipment detection, fault diagnosis, seismic exploration signal processing and other fields (Alsalah et al., 2021; Kumar and Chandra, 2023). It is worth noting that the presence of anomalous events in the signal to be processed can lead to modal aliasing and endpoint effects in the EMD (Wen, 2022). However, the seismic waveform used in this paper is a non-anomalous signal processed by SST noise reduction filtering, and no other anomalous microseismic events were generated for a period of time before and after this vibration, so using EMD to decompose the signal has a high confidence. The EMD first extracts the mean curve function  $m_{11}^{(0)}(t)$  of the upper and lower extreme envelopes within the mixed wave  $x(t)$ :

$$m_{11}^{(0)}(t) = \frac{e_{11}^{(0)}(t) + e_{u1}^{(0)}(t)}{2} \quad (1)$$

where  $e_{11}^{(0)}(t)$  and  $e_{u1}^{(0)}(t)$  are the upper and lower extremal envelopes of the signal to be resolved, respectively.

Then put the mixed wave function  $x(t)$  minus the mean curve  $m_{11}^{(0)}(t)$  to get a new function  $h_{11}^{(0)}(t)$ :

$$h_{11}^{(0)}(t) = x(t) - m_{11}^{(0)}(t) \quad (2)$$

Repeat the previous steps and consider the function  $h_{11}^{(0)}(t)$  as the original signal while updating the iteration order from 0 to 1. Let  $k$  be the number of iterations required for the function  $h_{1(k+1)}^{(k)}(t)$  to satisfy the intrinsic mode component condition, at which point  $h_{1(k+1)}^{(k)}(t) = \text{IMF}_1(t)$  is the first eigenmodal function:

$$h_{1(k+1)}^{(k)}(t) = h_{1k}^{(k-1)}(t) - m_{1(k+1)}^{(k)}(t) \quad (3)$$

The first IMF is separated from the mixing wave  $x(t)$  and the remaining signal is  $r_1(t)$ . Continue to repeat all the previous steps for  $r_1(t)$  to obtain each  $\text{IMF}_i(t)$  in turn until the final residual  $r_n(t)$ , which cannot be further decomposed, is obtained and the iteration is stopped:

$$r_n(t) = h_{n(k+1)}^{(k)}(t) - h_{(n-1)(k+1)}^{(k)}(t) \quad (4)$$

Eventually, the decomposition results of the mixed waveform consisting of S and P waves are shown in Fig. 5. IMF

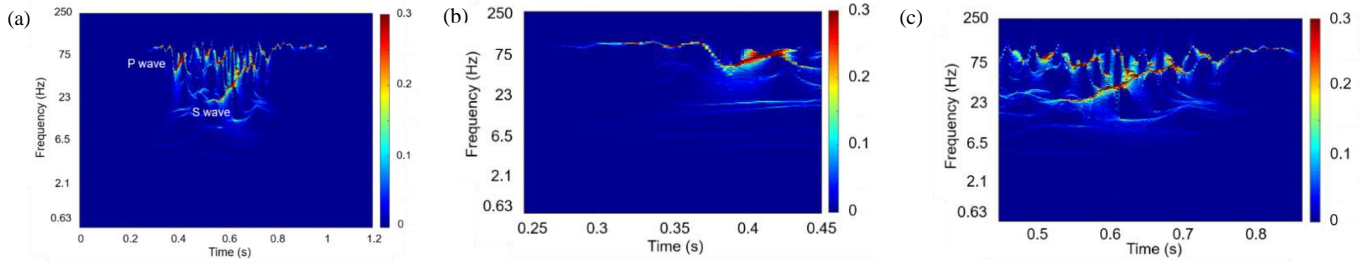


**Fig. 3.** T-F analysis of seismic wave through SST method (The color maps the signal energy on the T-F sampling points with high in red and low in blue). (a) Original wave spectrogram, (b) P wave spectrogram and (c) P/S mixed wave spectrogram (He et al., 2022).

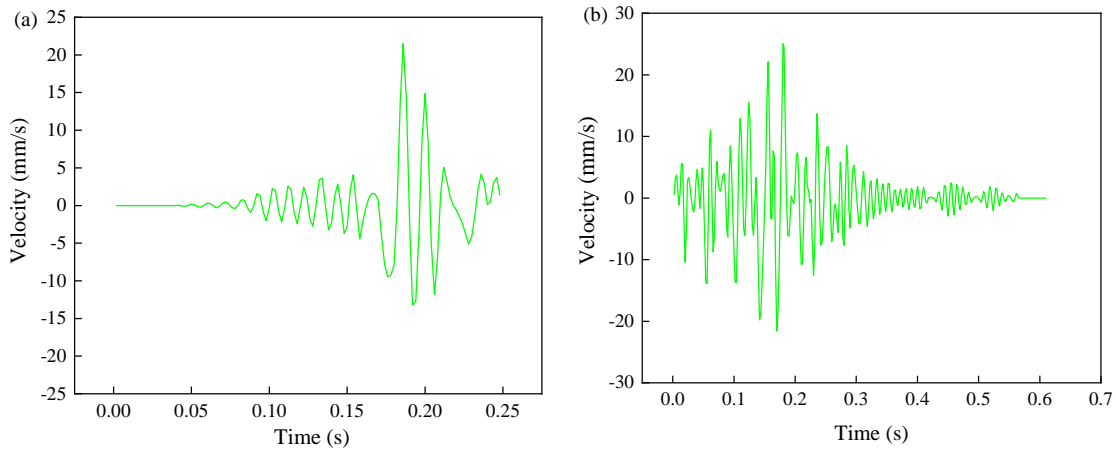


**Fig. 4.** Waveform filtered by SST. (a) P wave and (b) P/S mixed wave.

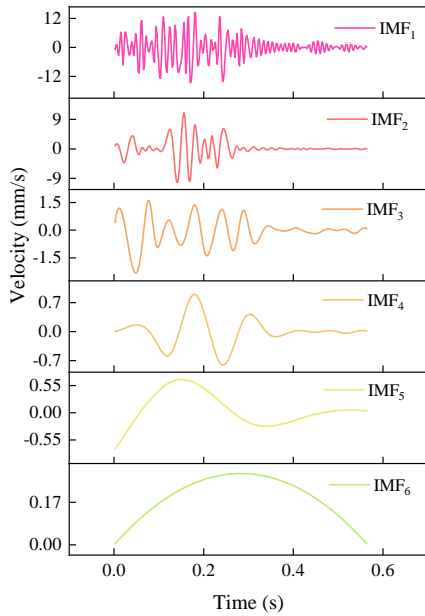


**Fig. 5.** Results of mixed waveforms decomposed by EMD.

waveforms are numbered based on their frequencies. IMF<sub>1</sub> has the highest frequency, while IMF<sub>6</sub> which has the lowest frequency is the residual amount.

The mutual information entropy measures the statistical dependence between two random variables. The higher dependence between two variables, the higher the entropy value. When the variables are more independent of each other, the entropy value is lower (Dheer and Majumdar, 2021). Its specific expression is:

$$I(X;Y) = -\sum_{x,y} p(x,y) \log \frac{p(x,y)}{p(x)p(y)} \quad (5)$$

where  $I$  is the mutual information entropy value,  $p(x,y)$  is the joint probability density function of two eigenmodal components,  $p(x)$  and  $p(y)$  denote the marginal probability density functions of two different eigenmodal components, respectively.

Due to amplitude and frequency differences between P and S waves, when the IMF components belong to the same wave, the entropy value is larger, and the entropy value is smallest at the location where P and S waves are separated.

Hence, the decomposed S wave component in the mixed waveform is:

$$S(t) = \sum_{i=1}^{b-1} \text{IMF}_i^S(t) \quad (6)$$

The decomposed P-wave component after S wave arrival is:

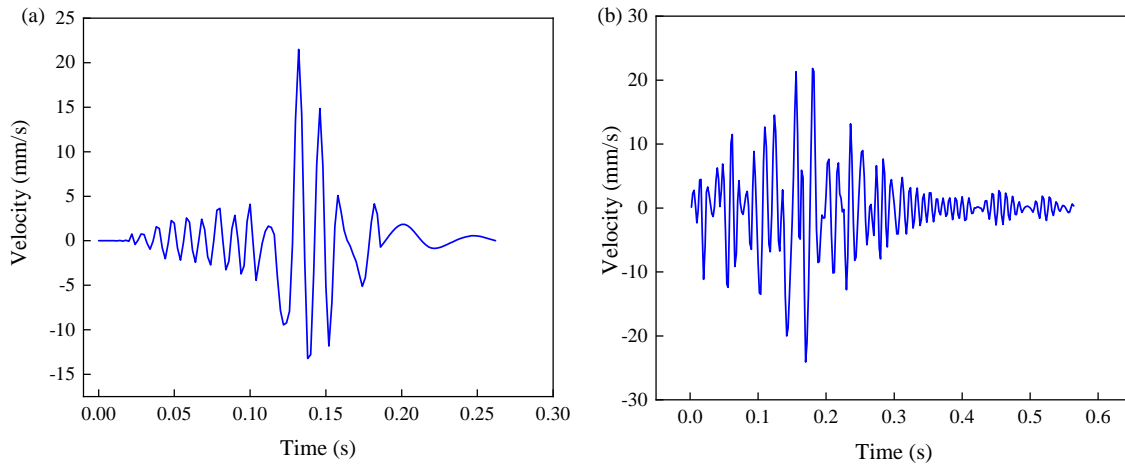


**Fig. 6.** Reconstructed waves by SST-EMD method. (a) P wave and (b) S wave.

$$L(t) = \sum_{i=b}^n \text{IMF}_i^P(t) \quad (7)$$

The complete P-wave waveform is:

$$P(t) = y(t) + L(t) \quad (8)$$

where  $\text{IMF}_i^S(t)$  is each intrinsic mode component of the S wave,  $\text{IMF}_i^P(t)$  is each intrinsic mode component of P wave, and  $y(t)$  is the P wave part before S wave arrival. The  $n$  is the total number of intrinsic mode components after removing the residuals, and  $b$  is the critical intrinsic mode component.

After calculation, the mutual information entropy values between adjacent IMF components from  $\text{IMF}_1$  to  $\text{IMF}_6$  are 0.76, 0.69, 0.71, 0.81, and 0.89, respectively. Therefore,  $\text{IMF}_{23}$  has the minimal value, representing the separation between P and S waves. This means that  $\text{IMF}_1$  and  $\text{IMF}_2$  belong to S wave, and  $\text{IMF}_3$ - $\text{IMF}_5$  are the components of the remanent P wave.

The decomposed P and S waves waveforms are eventually reconstructed using Eqs. (6)-(8) for each component signal, and the results are shown in Fig. 6. When compared to other waveform separation techniques in the field of geophysics, the most significant advantage of this method lies in its ability to effectively disentangle highly mixed transverse and longitudinal waves from single-component vibration wave signals monitored by mine microseismic systems. The developed method formed the groundwork for future accurate simulation of the rock stress and displacement field under the impacts of seismic waves.

### 3. Microseismic data and model construction

#### 3.1 Seismicity distribution

Seismic waves from coal and rock mass failure are the main source of dynamic load, which can be collected by microseismic monitoring system. The field seismic waves at different energy levels in Wudong coal mine are selected as dynamic inputs. Wudong coal mine is a typical rockburst-prone mine in Urumqi mining area, Xinjiang, China (He et

al., 2020). In recent years, 5 rockbursts and around 42,000 microseismic events have been monitored, with the maximum energy of microseismic events reaching  $7.1 \times 10^8$  J, causing severe roadway damage and economic losses. Figs. 7(a) and 7(b) show two rockbursts occurred at mining level +450, where microseismic events were significantly clustered prior to the accident. The “11.24” and “2.1” refer to the source of seismic events occurred on November 24<sup>th</sup>, 2016 and February 1<sup>st</sup>, 2017, respectively. The sources of rockbursts were mainly in the hard roof and the inter-seam rock pillar (Fig. 7(a)). Figs. 7(c) and 7(d) present the spatial distribution of microseismic events categorized into different energy levels. The distribution was plotted along the dip and strike of the working face at the +450 mining level, providing a visual representation of the event spatial clustering. Fig. 7(c) demonstrates that microseismic events generated within 40 m from the roadway sidewall account for about 95% of the total events. The microseismic events occurred more than 40 m from the roadway sidewall generally have energies below  $10^7$  J. It can be seen that the events within 440 m are mainly those with energy less than  $10^7$  J. The larger events with energies of  $10^8$ - $10^9$  are primarily distributed in the range of 1,060-2,025 m. Because the stronger and more frequent microseismic events had shorter distance to roadways, the roadway support system experienced significant deterioration and damage. Based on these results, the dynamic support design should be zoned spatially according to the intensity distribution of microseismic events. The same support design should not be applied along the whole roadway strike for support strength and cost considerations.

#### 3.2 FLAC3D model setup

FLAC3D 6.0 numerical modelling software was employed to conduct dynamic analysis on the roadway damage characteristics due to seismic waves for dynamic support design. A three-dimensional numerical model was constructed with dimensions of  $150 \times 150 \times 150$  m<sup>3</sup> (see Fig. 8). The length, width and height of the roadway located in model center were 150, 5 and 4 m, respectively. The meshes of the surrounding

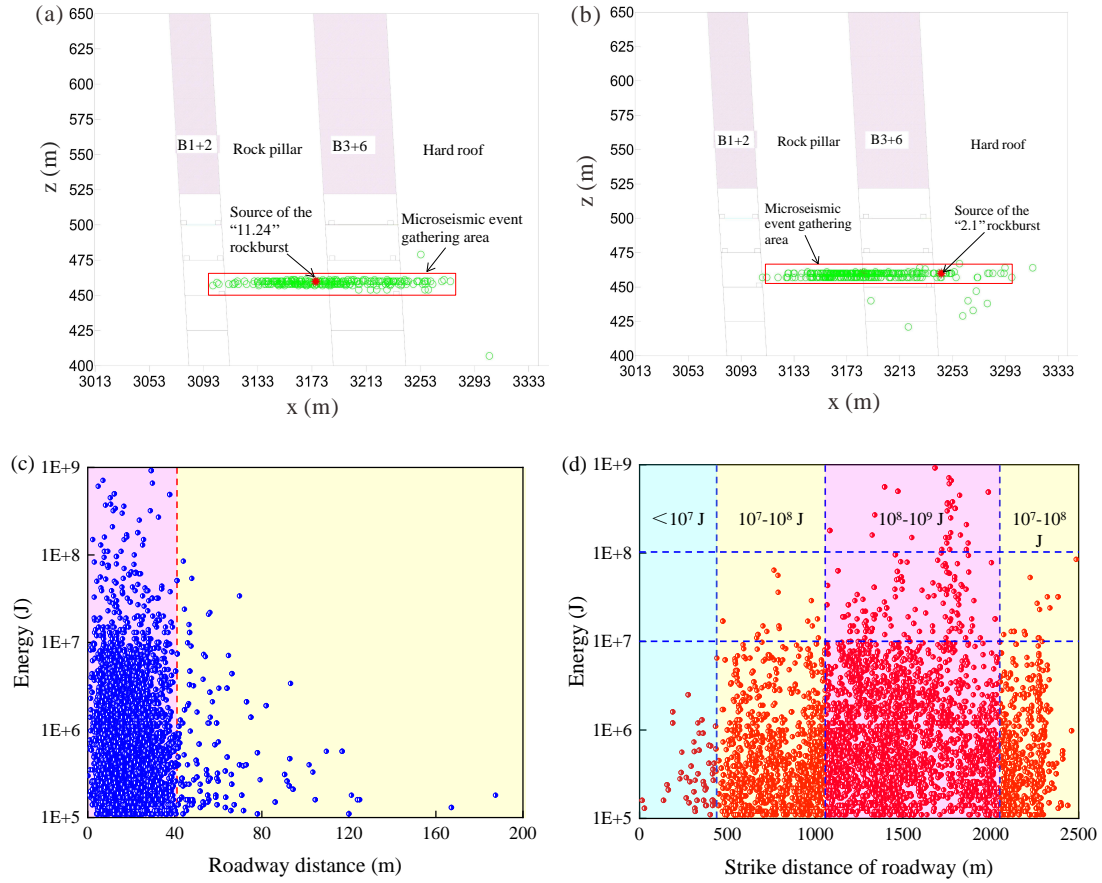


**Fig. 7.** Distribution of microseismic events in case study roadway. (a) Distribution of microseismic events before the “11.24” rockburst, (b) distribution of microseismic events before the “2.1” rockburst, (c) along dip direction and (d) along strike direction.

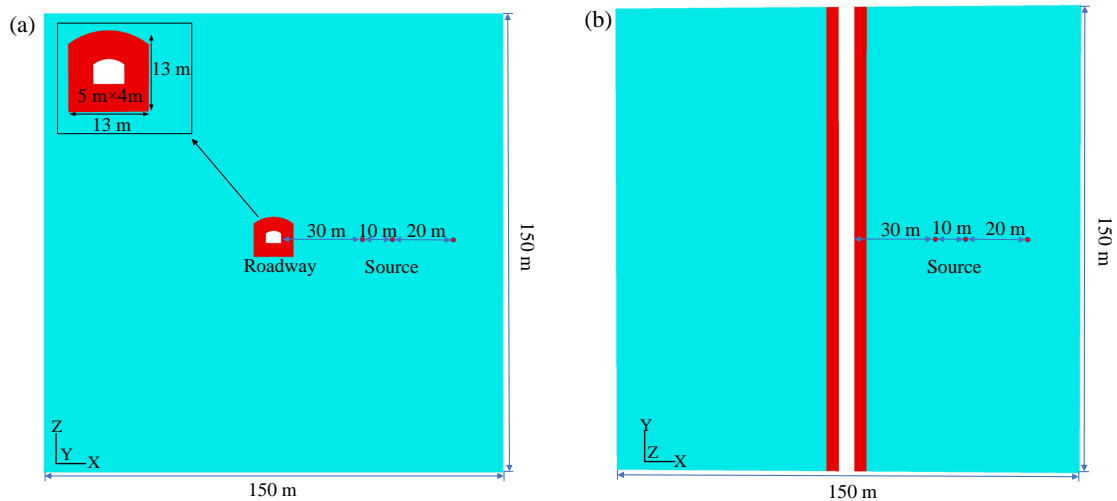


**Fig. 8.** Model used for dynamic simulation. (a) Sectional view and (b) plan view.

**Table 1.** Numerical simulation cases.

Case	Seismic source to roadway distance (m)	Source released seismic energy (J)	Dynamic loading
1	40	$10^7$	Decomposed wave
2	40	$10^8$	Decomposed wave
3	40	$10^9$	Decomposed wave
4	30	$10^8$	Decomposed wave
5	60	$10^8$	Decomposed wave
6	40	$10^8$	Mixed wave

rock (red area in Fig. 8) of the roadway are refined and the total number of nodes is 287,112 in the model. Fig. 7(c) revealed that microseismic events exceeding  $10^7$  J occurred mostly within 40 m of the roadway sidewalls. The farthest distance of the events above  $10^7$  J is about 60 m from the roadway. Hence, simplified spherical seismic sources are arranged at 30, 40 and 60 m away from the roadway sidewall for dynamic load application, as shown in Fig. 8.

Several cases are simulated to carry out parametric studies on the influence of seismic source-roadway distance and seismic magnitude on the ground reaction of the roadway surrounding rock mass, as described in Table 1. The decomposed P and S waveforms with the energy level of  $10^7$ ,  $10^8$ ,  $10^9$  J are applied at the spherical source in the normal and tangential oscillating directions, respectively. Also, a conventionally used mixed waveform with energy level of  $10^8$  J is applied in the normal direction (i.e., along the direction of wave propagation) of the spherical source for comparison.

### 3.3 Seismic load application

By incorporating the decomposed field seismic waveform, we guaranteed that the frequency and duration of the dynamic loads match those of the natural waveforms in our numerical study. To maintain a reasonable peak particle velocity (PPV) when modeling seismic wave propagating across the model from seismic sources with different energy levels, the scaling law was applied. McGarr (1984) put forward a scaling law that only relates to the energy level and source-target distance based on field data collected in underground mines. The scaling law has been widely used to estimate PPV for dynamic support design (Kaiser and Cai, 2012; Wang et al., 2016; Wang and Cai, 2017), the specific expression is:

$$PPV = \frac{C \times 10^{(a \cdot M_L)}}{r} \quad (9)$$

where  $M_L$  is the local magnitude of the seismic event, and  $\log E = 1.8 + 1.9M_L$ ,  $r$  is the source-target distance,  $a$  and  $C$  are site constants.

Kaiser and Maloney (1998) concluded that  $a$  could be fixed at 0.5 in most mines. In this study,  $C$  is 0.75 (He et al., 2022). Therefore, the estimated PPVs generated by seismic source with different energy levels and at different locations can be obtained using Eq. (9).

### 3.4 Material properties and boundary conditions

To investigate the yielding characteristics of the surrounding rock under the dynamic load, the surrounding rock (red area in Fig. 8) was set as the Mohr-Coulomb model. The rest of the host rock (blue-green area in Fig. 8) was set as the elastic model, which could achieve the fast propagation of P and S waves in the medium and allows prompt response to high loading rates in the dynamic simulation. The rock mechanical parameters were obtained based on the laboratory test results of rock samples from Wudong coal mine. For the mechanical parameters of the surrounding, the density, bulk modulus, shear modulus, cohesion and Friction are 2,813 kg/m<sup>3</sup>, 18.7 GPa, 10.7 GPa, 7.0 MPa, and 28.5°, respectively. The same density, shear modulus and bulk modulus were applied to the elastic part of the host rock.

In the static loading phase, all side boundaries of the model were fixed. The burial depth of the top surface of the model was 350 m. The magnitudes of horizontal and vertical stresses were applied as a function of burial depth derived by He et al. (2020). Quiet side boundaries were applied to the model during the dynamic loading phase to absorb the seismic waves propagating to the boundary. A calibrated damping coefficient of 6% was set to simulate the energy loss during the propagation of the seismic waves (He et al., 2022).

## 4. Results and discussion

### 4.1 Comparison of applying decomposed wave and mixed wave

#### 4.1.1 Velocity analysis

In case 2, the decomposed P and S waves were amplified to  $10^8$  J energy and applied to a seismic source 40 m away from the roadway. The P and S waves oscillations were applied in the normal and tangential directions of the propagation path respectively to simulate the theoretical oscillations of P and S waves. As shown in Figs. 9(a) and 9(b), in the dynamic calculation, 0-0.2 s, 0.2-0.26 s, and 0.26-0.63 s are the loading phases of P wave, P/S waves, and only S wave, respectively. During the loading phase of P wave, the horizontal velocity was dominant compared to the vertical velocity. However, when S wave started loading, the vertical particle velocity was much greater than that in the horizontal direction. This phenomenon was more obvious on the sidewall (see Fig.

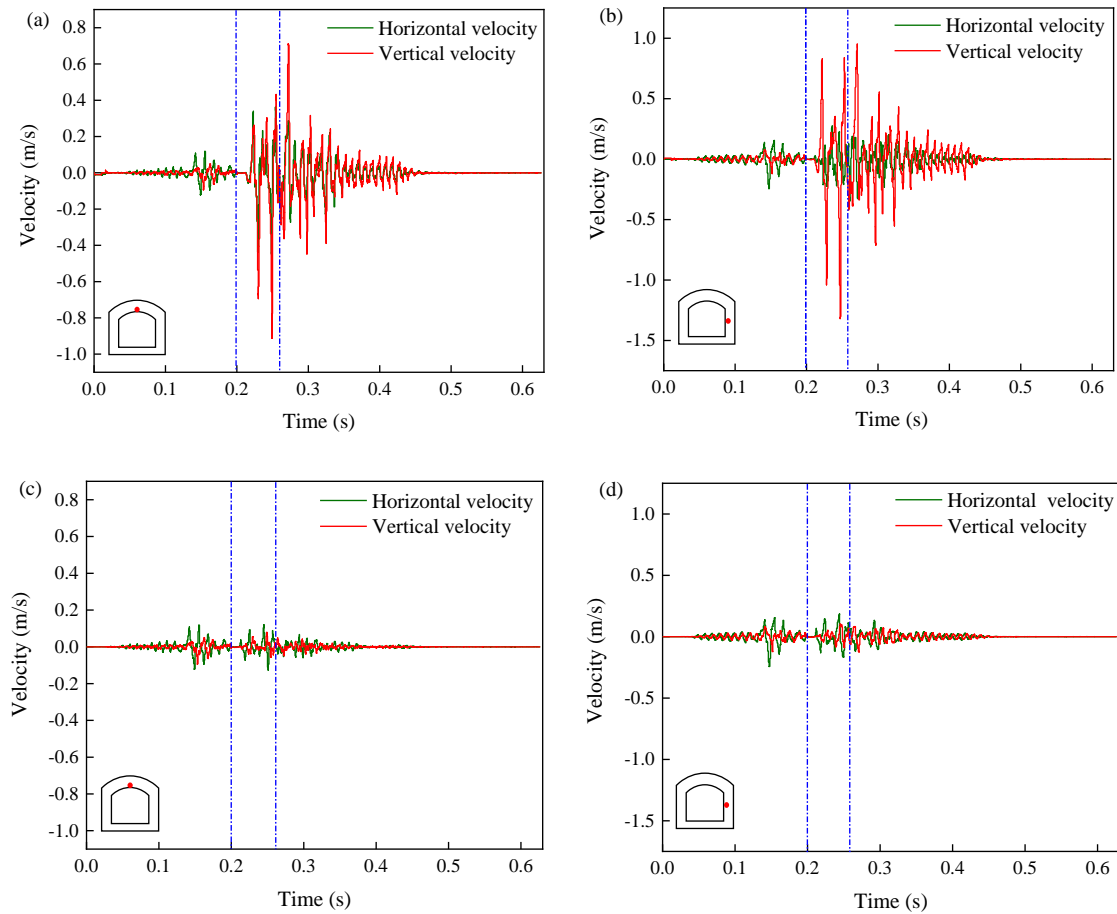


**Fig. 9.** Particle velocity monitoring results in case 2 and case 6. (a) Roof monitoring point (case 2), (b) sidewall monitoring point (case 2), (c) roof monitoring point (case 6) and (d) sidewall monitoring point (case 6).

9(b)) when monitoring point was at the same level with the seismic source. Additionally, these results demonstrated that P waves, with their vibrations aligned with the direction of wave propagation, were responsible for damaging the sidewalls of the roadway. On the other hand, S waves, characterized by their vertical vibrations, induced greater vertical velocity in the roadway's roof.

When it comes to case 6, it applies the same seismic wave as in case 2 at the source location, but both P and S waves are applied along the direction of wave propagation. Figs. 9(c) and 9(d) present the monitored particle velocity on the sidewall and the roof, respectively. The velocity results are consistent with case 2 in the P wave loading phase (0-0.2 s), however, the velocity of particle vibration in the vertical direction is slightly less than that in the horizontal direction after the P wave loading phase, and the wave velocity in vertical direction is also much lower than that in case 2. It can be seen that the monitored wave velocity results using mixed wave do not show many differences in directionality. Therefore, the differentiated oscillation patterns of P and S waves in case 2 shows the advantage of applying SST-EMD decomposed seismic wave in the dynamic loading simulation.

#### 4.1.2 Displacement characteristics

The monitored displacements of the roadway roof and the sidewall are shown in Fig. 10. In case 2, when incident P wave comes, the sidewall of the roadway deformed significantly in horizontal direction towards the free face and did not rebound (Fig. 10(b)), indicating that the rock mass has already failed. Under the mixed P/S wave loading disturbance (0.2-0.26 s), the sidewall rock was significantly displaced in the horizontal direction, and the vertical displacement was characterized by significant elastic fluctuations until it finally stabilized. Since the S wave started loading, the rock mass on the roof (Fig. 10(a)) shows significant displacement changes in the vertical direction and less fluctuation of horizontal displacement. In the S wave loading phase alone (0.26-0.63 s), the roof and sidewall displacements of the roadway increased only slightly compared with the mixed P/S wave loading phase, but the displacement changes stabilized in the later part of this phase, indicating that plastic damage of the surrounding rock happened. The roof of the roadway is more sensitive to the vertical displacement response, while in the horizontal displacement is more active at the sidewall location. In general, the seismic wave propagation through the medium, the role of the surrounding rock to lead to changes in the distance

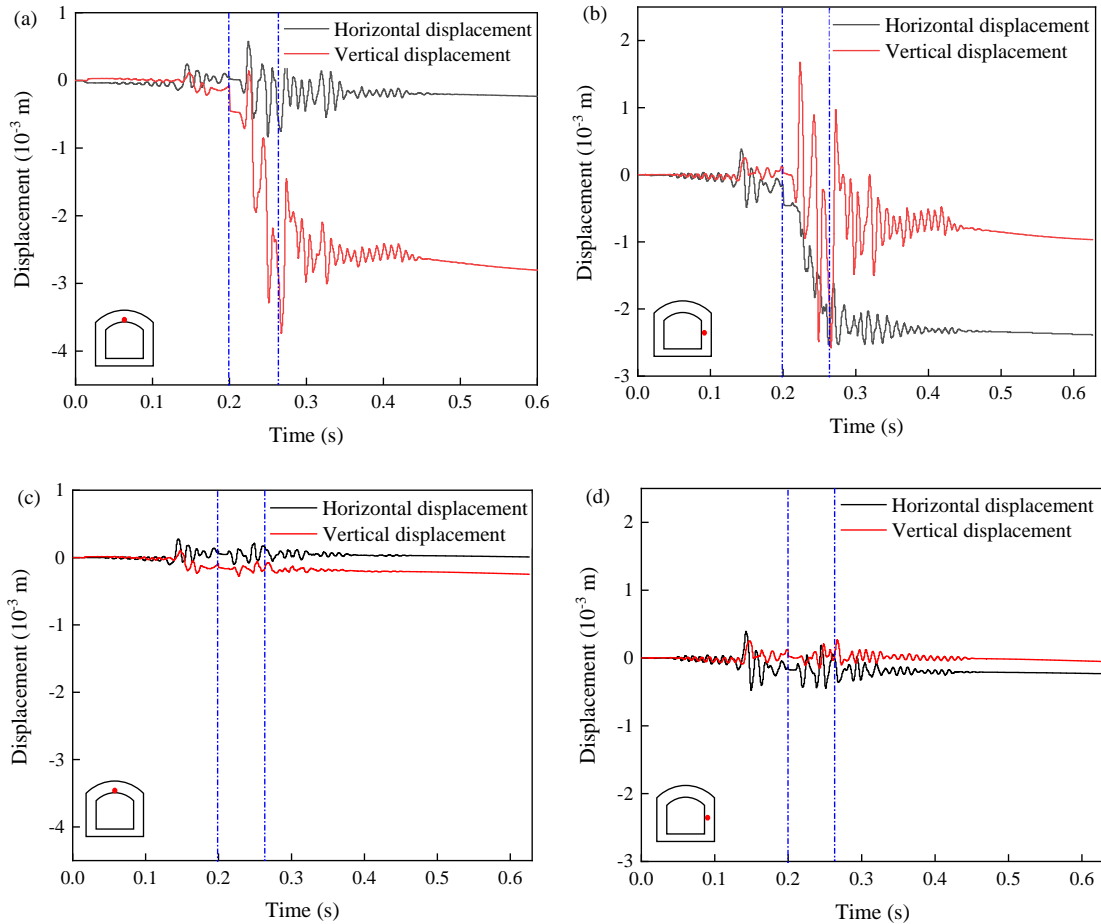


**Fig. 10.** Displacements calculation results around roadway under different dynamic wave applying method. (a) Roof monitoring point (case 2), (b) sidewall monitoring point (case 2), (c) roof monitoring point (case 6) and (d) sidewall monitoring point (case 6).

between its mass, the greater the change in distance, the greater the displacement of the position. The transverse wave due to their own vertical propagation direction vibration mode is more likely to cause greater vibration of the mass of the point. As for case 6, there was only minor displacement at each measurement point, and did not show the displacement difference characteristic between P wave and S wave (Figs. 10(c) and 10(d)).

#### 4.1.3 Yielding zone development

The superposition of static and dynamic seismic loads leads to plastic damage of the surrounding rock when it exceeds the critical threshold for the rock damage. The results of Mohr-Coulomb yielding zone of cases 2 and 6 are shown in Fig. 11. It can be seen from Fig. 11(a) that the surrounding rock of the roadway has already suffered certain degree of damage after excavation, and the plastic yielding zone further developed on the sidewall after P wave arrival in Fig. 11(b). After S wave loading, Fig. 11(c) shows that the incident disturbance caused significant plastic damage to the upper right corner of the roadway, as well as the roof and right sidewall in case 2. In case 6, the mixed wave only causes minor damage

to the sidewall of the roadway. In order to more visually demonstrate the damage results of the surrounding rock under different loading methods, the volume of the plastic zone of the roadway surrounding rock after P and S waves loading was statistically calculated, and the results are shown in Table 2. In case 2, the total volume of plastic failure caused during S wave loading reached  $237.91 \text{ m}^3$ , which accounted for 83.8% of total failure volume. This is in consistent with the existing findings that S wave have larger PPV and tend to cause greater damage (Kaiser et al., 1996; Li et al., 2020b). As for case 6, only 0.8% of the plastic damage occurred in S wave loading phase. Therefore, according to the comparison of the velocity, displacement and yielding results in two cases, applying SST-EMD decomposed P and S waves is more reasonable and closer to reality than using a mixed wave.

## 4.2 The influence of seismic source energy

### 4.2.1 Rockmass yielding results

Since the damage results produced by seismic waves at various energy levels are inconsistent, this study takes the three large energy level events occurring in the case mine as the

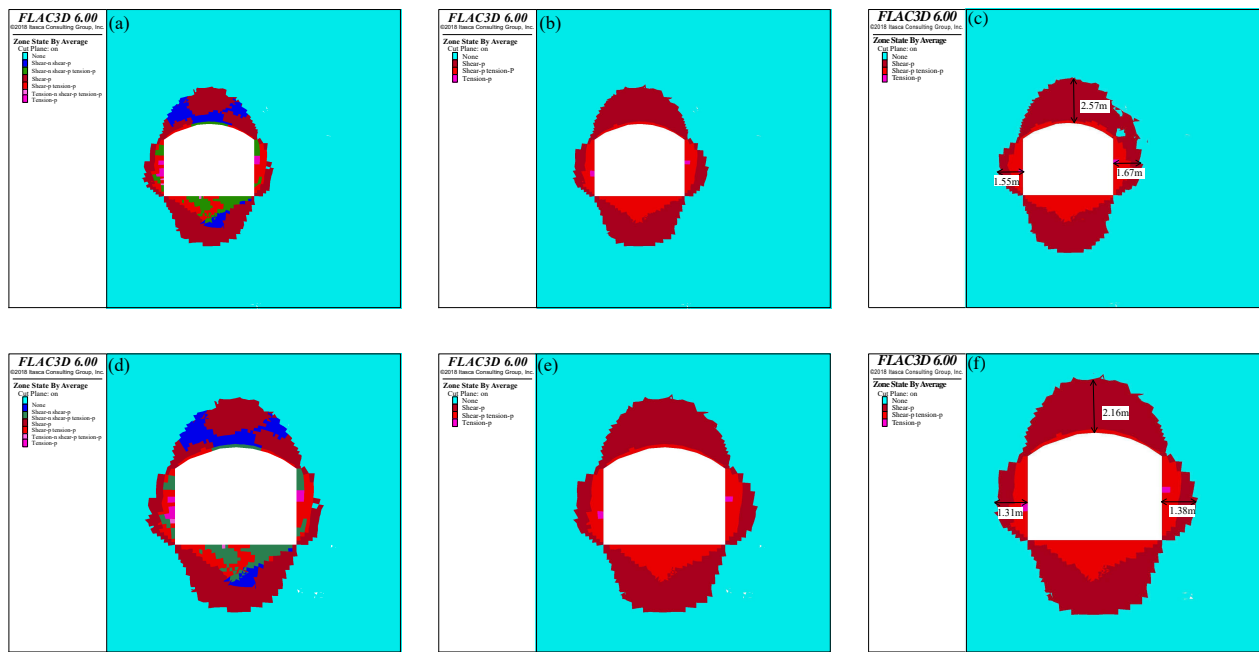


**Fig. 11.** The yielding zone development results at different stages. (a) Static (case2), (b) after P wave (case2), (c) after S wave (case 2), (d) static (case 6), (e) after P wave (case 6) and (f) after S wave (case 6).

**Table 2.** Comparison of rock damage around roadway with case 2 and case 6.

Case	Dynamic loading	Damaged volume caused by P wave (m <sup>3</sup> )	Percentage by P wave (%)	Damaged volume caused by S wave (m <sup>3</sup> )	Percentage by S wave (%)
2	Decomposed wave	46.16	16.2	237.91	83.8
6	Mixed wave	46.16	99.2	0.374	0.8

target energy levels in purpose of studying the damage law of the roadway surrounding rock under the action of varying energy levels. Compared with the yielding zone caused by seismic energy of  $10^8$  J in case 2, Fig. 12 shows yielding zone results caused by different seismic energy levels ( $10^7$  and  $10^9$  J). It was found when the source energy level of  $10^7$  J in case 1 only caused minor plastic damage to the sidewall near on the source side. As the seismic energy level increases to  $10^9$  J in case 3, rock failure occurred on the roof, sidewall, and upper right corner of the roadway, as shown in Fig. 12(b). Using the self-programmed FISH program to extract the plastic damage volume from the model, it was found that removing the plastic damage caused by the roadway excavation, the rock yielding volume reaches 658.8 m<sup>3</sup> in case 3, while the volume is only 102.7 m<sup>3</sup> when seismic energy level is  $10^7$  J. Therefore, the potential seismic event magnitude is an important consideration in roadway dynamic support design. When designing the roadway support, the probability of maximum seismic energy that may occur near the roadway must be considered based on seismic monitoring data analysis and geological exploration, so as to avoid the inadequate support effect.

According to Kaiser and Cai (2013), extreme ground motions caused by S wave should be carefully taken into

account when designing roadway dynamic support. Thus, the statistical analysis is performed on the rock damage volume caused by P and S waves of different energy levels, as shown in Fig. 13. It can be seen when the seismic energy level is  $10^7$  J, the rock damage caused by the S wave accounts for 75.8%, whereas the P wave only led to 24.2% of the damage. With the increment of the seismic energy level at the source, the proportion of damage to the surrounding rock caused by S wave increases, reaching 85.8% when the energy level is  $10^9$  J. This is in line with the analysis by Yan et al. (2020) that S wave lead to much greater damage to the rock mass than P wave.

#### 4.2.2 Displacement characteristics

In this section, the influence of different energy levels of the seismic source on the surrounding rock displacements is analyzed. Figs. 14(b) and 14(d) show the horizontal and vertical displacements of the rock mass on the roadway sidewall during dynamic loading. It can be observed that horizontal displacements on the sidewall increase dramatically with higher seismic energy. In case 1, the horizontal displacement on the sidewall is slightly larger than the vertical displacement, whereas it is almost four times larger than the vertical displacement in case 3. On the roadway roof, the ver-

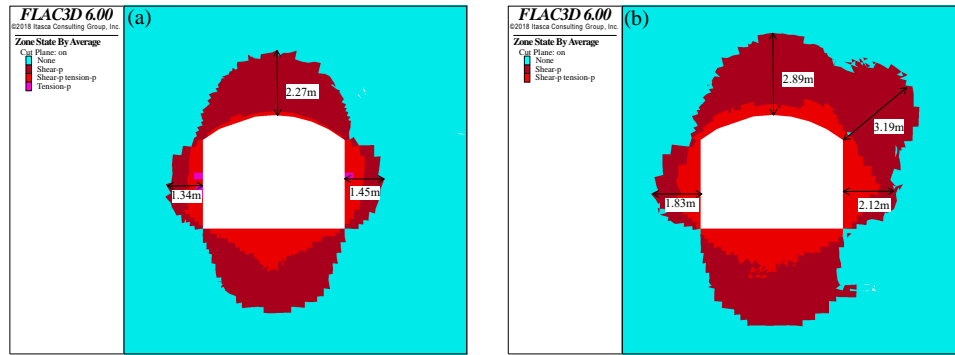


**Fig. 12.** Damage of roadway with different source energy levels. (a) After S wave (case 1) and (b) after S wave (case 3).

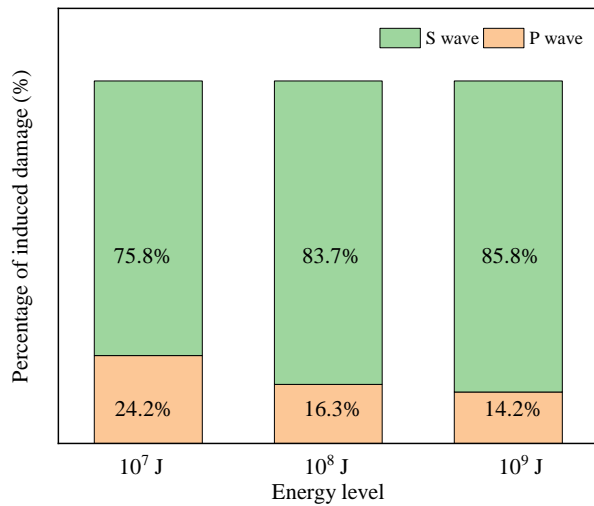


**Fig. 13.** Rock damage percentages caused by P and S waves with different seismic energy levels.

tical displacements also increase significantly with a higher input seismic energy (see Figs. 14(a) and 14(c)). The horizontal and vertical displacements around the roadway caused by case 2 are 4.2 and 2 times greater than those caused by case 1, respectively, whereas these values are 11.6 and 3.5 times greater in case 3. This indicates that the surrounding rock displacements increase rapidly with higher seismic energy level in the far field, and as a result, the surrounding rock is more likely to fall or eject violently under dynamic disturbance.

#### 4.3 Influence of seismic source location on roadway ground reaction

Fig. 15 depicts yielding zone developments of the roadway caused by seismic sources at different distances. The extent of the yielded zone around the roadway grows dramatically as the seismic source-roadway distance decreases. When the dynamic load source is located far from the roadway, it primarily damages the sidewall on the source side (case 5). The displacement and rock yield conditions under different source-roadway distances are summarized in Table 3. With the decrease of the distance between the seismic source and roadway, the rock yielding around roadway increases significantly. This is

due to the rock damping effect, which means that the longer traveling distance of the seismic wave, the lower residual energy of the incident waves around the roadway, leading to a decreasing disturbance to the surrounding rock. The damage to the surrounding rock caused by the S wave is dominant in all three cases, ranging from 56.1% to 83.7% of the total rock damage. It is noteworthy that the percentage of S wave damage increases and then decreases with increasing source-roadway distance, and the largest damage percentage of S wave was found at the location of the source 40 m from the roadway. This indicates the existence of S wave critical damage distance, beyond which both the total damage and the percentage of S wave damage in the rock will decrease.

#### 5. Roadway dynamic support optimization

As the mining depth increases, the surrounding rock of the roadway gradually enters a dynamic and static load superimposed stress environment with strong dynamic disturbances. Thus, it is critical to design an anti-seismic loading support scheme to ensure the safe production of mines under dynamic disturbance. The fitting results of calculated PPV values generated by different seismic loads in FLAC3D are shown in Fig. 16. The PPV value curve is steeper and the seismic wave attenuation speed increases with increasing energy level. The results show different roadway damage ranges by using PPV of 0.55 m/s as the rockburst damage threshold (He et al., 2020). The roadway damage ranges caused by seismic source energies of  $10^7$ ,  $10^8$  and  $10^9$  J are approximately 8, 27 and 40 m, respectively.

The yielding zone depths under different energy levels of seismic loadings are shown in Figs. 11(c), 12(a) and 12(b). The yielding zone around the roadway increases with higher energy level. The maximum yielding depths are 2.3, 2.6 and 3.2 m in the roof and 1.5, 1.7 and 2.2 m in the sidewall, caused by seismic energies of  $10^7$ ,  $10^8$  and  $10^9$  J, respectively. Li (2021) suggested the bolt length in the roadway support system should be at least 1 m longer than the yielding zone. Thus, the current support length of 2.5 m in the case study mine cannot meet the roadway support requirements under the seismic disturbances, which can be the root cause for the frequent appearance of sidewall heave after mining-induced seismicity, as shown Fig. 17. Combined with the above analysis, the relationship between

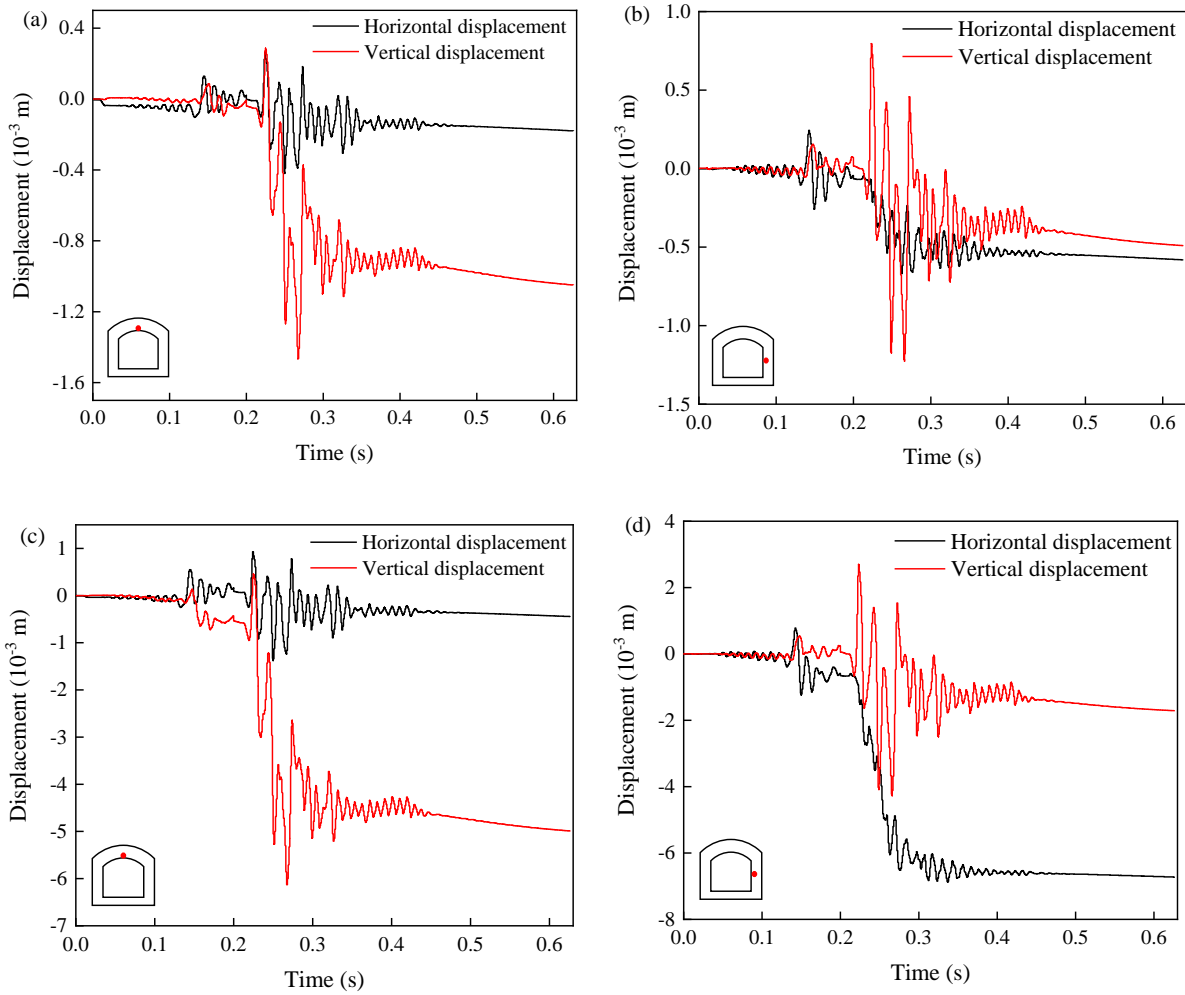


**Fig. 14.** Surrounding rock displacement with different seismic energy levels. (a) Roof monitoring point (case 1), (b) sidewall monitoring point (case 1), (c) roof monitoring point (case 3) and (d) sidewall monitoring point (case 3).

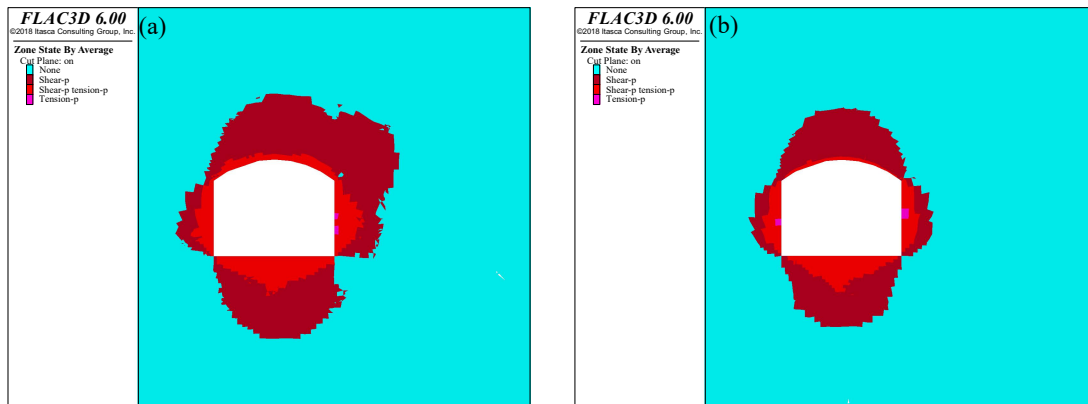


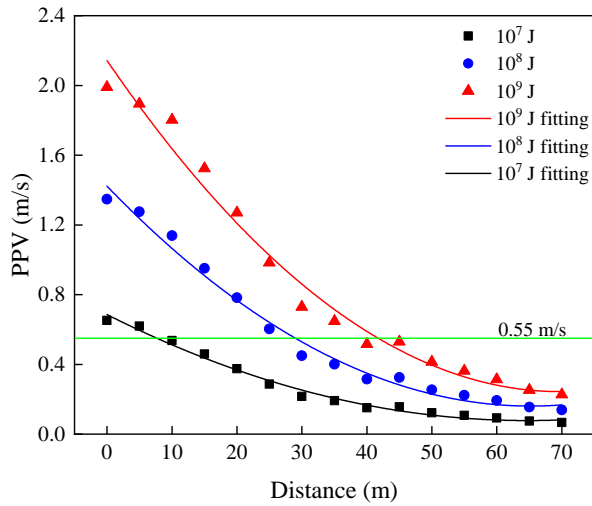
**Fig. 15.** The yielding zone development results. (a) After S wave (case 4) and (b) after S wave (case 5).

**Table 3.** Damage of roadway with different source-roadway distances.

Case	Source-roadway distance (m)	Sectional yielded depth (m)	Total yielded volume (m <sup>3</sup> )	P wave percentage of damage (%)	S wave percentage of damage (%)
4	30	3.2	656.5	25.9	74.1
2	40	2.5	284.1	16.3	83.7
5	60	2.1	179.2	43.9	56.1

**Table 4.** Optimized dynamic support scheme.

Seismic energy level	Bolt spacing (m)	Roof bolt length (m)	Left sidewall bolt length (m)	Right side bolt length (m)	Number of anchor cables
10 <sup>7</sup> J	0.7	3.3	2.5	2.5	3
10 <sup>8</sup> J	0.6	2.7, 3.8	2.7	2.8	3
10 <sup>9</sup> J	0.4	3.4, 4.5	3.0	3.3, 4.5	4

**Fig. 16.** PPV value variation curve with distance.

en the length  $R$  of the plastic zone of the surrounding rock under the action of P-wave and S-wave and the length  $L$  of the anchor support is as follows:

$$L = R_i + 1 \quad (10)$$

where  $R_i$  is the length of plastic zone development at each location of the roadway.

Based on the FLAC3D modelling and seismicity distribution at different positions (Fig. 7(d)), the roadway in the case study mine can be divided into three zones with different damage characteristics based on their seismic activity, i.e., the subjected seismic energy below 10<sup>7</sup> J, between 10<sup>7</sup>-10<sup>8</sup> J, and between 10<sup>8</sup>-10<sup>9</sup> J. The minimum bolt spacing of roadway support can be obtained for each zone using the following equation, which was suggested for roadway support system at burst-prone mines (Li, 2021):

$$s^2 = \frac{1}{F} \frac{2W_{rs}}{R\rho v^2} \quad (11)$$

where  $s$  is the spacing of the bolts,  $R$  is the rock damage depth,  $\rho$  is the density of the rock mass,  $W_{rs}$  is the energy

absorption of the support system,  $F$  is the factor of safety, specifically,  $F = W_{rs}/W_k > 1$ ,  $W_k$  is the energy of the ejected rock,  $W_k = (mv^2)/2$ ,  $m$  is the mass of the ejected rock,  $v$  is the ejection velocity, which can be back calculated based on the horizontally displacement of the ejected rock (Kaiser et al., 1996).

The calculated bolt spacings for roadway sections subjected to microseismic energy of 10<sup>7</sup>, 10<sup>8</sup>, 10<sup>9</sup> J energy are 0.7, 0.6 and 0.4 m, respectively. Hence, by combining Eq. (10) to determine the anchor length required to maintain the stability of the roadway envelope under P/S wave oscillation, the final “zoned and asymmetric” dynamic support scheme for this case study mine roadway is shown in Fig. 18. Table 4 summarizes the information on the length and number of anchors for different support systems in the support scheme. All anchor cables in the support system (dashed lines in Fig. 18) are 10 m long and are arranged perpendicular to the roadway. The designed support scheme not only addresses the asymmetric damage of the roadway surrounding rock under different seismic wave energy levels, but also considers the seismic energy distribution along the strike of the roadway. Furthermore, mines that frequently face dynamic disturbances can draw valuable insights from the anti-dynamic load support method outlined in this paper. This method focuses on the distribution characteristics of microseismic events and the prediction of rock damage caused by seismic waves. Ultimately, this approach can provide effective guidance for roadway support in the presence of dynamic loads, as well as leading to enhanced cost-efficiency through targeted and zoned support design.

## 6. Conclusions

In this paper, the problem of decomposition and reconstruction of transverse and longitudinal waves from single-component sensors was addressed. Combined with the spatial distribution of microseismic energy levels and the predicted damage characteristics of rock mass via dynamic modeling, a “zoned and asymmetric” dynamic support scheme was proposed for the case study mine. The main conclusions are



**Fig. 17.** Damage characteristics of roadway sidewall heave under large energy seismic.

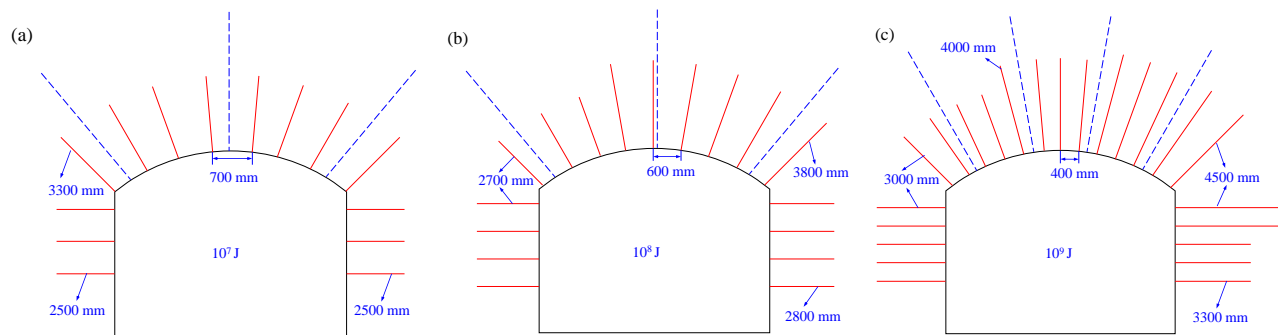


**Fig. 18.** Roadway support scheme of different areas. (a)  $10^7$  J support scheme, (b)  $10^8$  J support scheme and (c)  $10^9$  J support scheme.

as follows:

- 1) The proposed SST-EMD method fully decomposed naturally mixed microseismic waveforms into P and S waves. This advancement offers a more authentic dynamic load input for modeling of mining-induced microseismic events. As a result, the precision in terms of wave oscillation directions and ground reactions in our dynamic modeling was increased.
- 2) The horizontal particle velocity was dominant during the P wave oscillation phase, while the vertical vibration velocity showed a remarkable increase after the onset of S wave. These modeling results demonstrated a rational directional characteristics of the simulated particle movement under seismic loading.
- 3) Under the influence of decomposed P and S waves, vertical displacement greatly exceeded horizontal displacement at the roadway back, whereas the sidewalls exhibited the opposite behavior. The PPV, displacement and plastic yielding of the roadway surrounding rock positively scaled with the seismic energy level, and were inversely related to the source-roadway distance.
- 4) Based on the microseismic energy distribution analysis and predicted damage of surrounding rock under different dynamic loads, a “zoned and asymmetric” dynamic support method was proposed for the roadway, which provides guidance for avoiding excessive support strength or insufficient support effect during support design in

burst-prone mines.

## Acknowledgements

This work was financially supported by the National Natural Science Foundation of China (No. 52204197), the Post-doctoral Research Foundation of China (No. 2021M700371), the Fundamental Research Funds for the Central Universities (Nos. QNXM20220005, FRF-TP-22-111A1), the Ministry of Education’s ‘Chunhui Plan’ Collaborative Research project (No. 202200438).

## Conflict of interest

The authors declare no competing interest.

**Open Access** This article is distributed under the terms and conditions of the Creative Commons Attribution (CC BY-NC-ND) license, which permits unrestricted use, distribution, and reproduction in any medium, provided the original work is properly cited.

## References

- Alsalah, A., Holloway, D., Mousavi, M., et al. Identification of wave impacts and separation of responses using EMD. *Mechanical Systems and Signal Processing*, 2021, 151: 107385.
- Basarir, H., Sun, Y., Li, G. Gateway stability analysis by global-local modeling approach. *International Journal of Rock Mechanics and Mining Sciences*, 2019, 113: 31-40.
- Chu, H., Ma, T., Zhu, W., et al. A novel semi-analytical mon-

- itoring model for multi-horizontal well system in large-scale underground natural gas storage: Methodology and case study. *Fuel*, 2023a, 334, 126807.
- Chu, H., Zhang, J., Zhang, L., et al. A new semi-analytical flow model for multi-branch well testing in natural gas hydrates. *Advances in Geo-Energy Research*, 2023b, 7(3), 176-188.
- De Lauro, E., De Martino, S., Falanga, M., et al. Fast wavefield decomposition of volcano-tectonic earthquakes into polarized P and S waves by Independent Component Analysis. *Tectonophysics*, 2016, 690: 355-361.
- Dhamne, R. R., Mishra, S., Kumar, A., et al. Deformation behavior of D-Shaped shallow tunnels under dynamic loading conditions. *Structures*, 2021, 33: 3973-3983.
- Dheer, P., Majumdar, K. K. A nonparametric algorithm for estimating mutual information between digital signals. *Digital Signal Processing*, 2021, 116: 103111.
- Emad, M. Z., Mitri, H., Kelly, C. Dynamic model validation using blast vibration monitoring in mine backfill. *International Journal of Rock Mechanics and Mining Sciences*, 2018, 107: 48-54.
- Fan, Z., Zhang, J., Xu, H. Theoretical study of the dynamic response of a circular lined tunnel with an imperfect interface subjected to incident SV-waves. *Computers and Geotechnics*, 2019, 110: 308-318.
- Feng, J., Wang, E., Huang, Q., et al. Experimental and numerical study of failure behavior and mechanism of coal under dynamic compressive loads. *International Journal of Mining Science and Technology*, 2020, 30(5): 613-621.
- Feng, J., Wang, E., Shen, R., et al. A source generation model for near-field seismic impact of coal fractures in stress concentration zones. *Journal of Geophysics and Engineering*, 2016, 13(4): 516-525.
- Forbes, B., Vlachopoulos, N., Diederichs, M. S., et al. Augmenting the in-situ rock bolt pull test with distributed optical fiber strain sensing. *International Journal of Rock Mechanics and Mining Sciences*, 2020, 126: 104202.
- Ghaychi Afrouz, S., Westman, E., Dehn, K., et al. Underground rock mass behavior prior to the occurrence of mining induced seismic events. *Geotechnics*, 2022, 2(3): 765-780.
- Ghorbani, M., Shahriar, K., Sharifzadeh, M., et al. A critical review on the developments of rock support systems in high stress ground conditions. *International Journal of Mining Science and Technology*, 2020, 30(5): 555-572.
- He, S., Chen, T., Song, D., et al. A new methodology for the simulation of tunnel rockburst due to far-field seismic event. *Journal of Applied Geophysics*, 2022, 202: 104651.
- He, S., Chen, T., Vennes, I., et al. Dynamic modelling of seismic wave propagation due to a remote seismic source: A case study. *Rock Mechanics and Rock Engineering*, 2020, 53(11): 5177-5201.
- Herrera, R. H., Tary, J. B., Baan, M. V. D., et al. Body wave separation in the time-frequency domain. *IEEE Geoscience and Remote Sensing Letters*, 2014, 12(2): 364-368.
- Hosseinzadehsabeti, E., Ferré, E. C., Persaud, P., et al. The rupture mechanisms of intraslab earthquakes: A multi-scale review and re-evaluation. *Earth-Science Reviews*, 2021, 221: 103782.
- Kaiser, P. K., Cai, M. Design of rock support system under rockburst condition. *Journal of Rock Mechanics and Geotechnical Engineering*, 2012, 24: 215-227.
- Kaiser, P. K., Cai, M. Critical review of design principles for rock support in burstprone ground-time to rethink! *Australian Centre for Geomechanics*, 2013, 4(3): 3-37.
- Kaiser, P. K., Maloney, S. M. Scaling laws for the design of rock support. *Pure and Applied Geophysics*, 1998, 415-434.
- Kaiser, P. K., Tannant, D. D., McCreath, D. R. Canadian rockburst support handbook. Sudbury, Ontario: Geomechanics Research Centre. Sudbury, Laurentian University, 1996.
- Kim, J. S., Lee, C., Kim, G. Y. Estimation of damage evolution within an in situ rock mass using the acoustic emissions technique under incremental cyclic loading. *Geotechnical Testing Journal*, 2021, 44(5): 1358-1378.
- Kumar, A., Chandra, M. Empirical mode decomposition based statistical features for discrimination of speech and low frequency music signal. *Multimedia Tools Applications*, 2023, 82(1): 33-58.
- Lamur, A., Kendrick, J. E., Schaefer, L. N., et al. Damage amplification during repetitive seismic waves in mechanically loaded rocks. *Scientific Reports*, 2023, 13(1): 1271.
- Li, C. Principles and methods of rock support for rockburst control. *Journal of Rock Mechanics and Geotechnical Engineering*, 2021, 13(1): 46-59.
- Li, S., Li, C., Yao, D., et al. Using GPS and InSAR data to assess the cumulative damage of an underground utility tunnel. *Arabian Journal of Geosciences*, 2020a, 13: 62-74.
- Li, Z., Liang, G., Gu, B. Improved method of separating P- and S-waves using divergence and curl. *Chinese Journal of Geophysics*, 2013, 56(6): 2012-2022. (in Chinese)
- Li, C., Wu, Z., Zhang, W., et al. A case study on asymmetric deformation mechanism of the reserved roadway under mining influences and its control techniques. *Geomechanics and Engineering*, 2020b, 22(5): 449-460.
- McGarr, A. Scaling of ground motion parameters, state of stress, and focal depth. *Journal of Geophysical Research-Solid Earth*, 1984, 89(B8): 6969-6979.
- Mishra, S., Kumar, A., Rao, K. S., et al. Experimental and numerical investigation of the dynamic response of tunnel in soft rocks. *Structures*, 2021, 29: 2162-2173.
- Mishra, S., Zaid, M., Rao, K. S., et al. FEA of urban rock tunnels under impact loading at targeted velocity. *Geotechnical and Geological Engineering*, 2022, 40(4): 1693-1711.
- Mitelman, A., Elmo, D. Analysis of tunnel support design to withstand spalling induced by blasting. *Tunneling and Underground Space Technology*, 2016, 51: 354-361.
- Morissette, P., Hadjigeorgiou, J., Thibodeau, D. Assessment of support performance under dynamic loads at Vale Creighton Mine. Paper ARMA-11-288 Paper presented at the 45<sup>th</sup> U.S. Rock Mechanics/Geomechanics Sympos-

- sium, San Francisco, California, 26-29 June, 2011.
- Perazzelli, P., Anagnostou, G. Stress analysis of reinforced tunnel faces and comparison with the limit equilibrium method. *Tunneling and Underground Space Technology*, 2013, 38: 87-98.
- Ranjith, P. G., Zhao, J., Ju, M., et al. Opportunities and challenges in deep mining: a brief review. *Engineering*, 2017, 3(4): 546-551.
- Rodríguez, R., Díaz-Aguado, M. B. Deduction and use of an analytical expression for the characteristic curve of a support based on yielding steel ribs. *Tunneling and Underground Space Technology*, 2013, 33: 159-170.
- Sabagh, M., Ghalandarzadeh, A. Centrifugal modeling of continuous shallow tunnels at active normal faults intersection. *Transportation Geotechnics*, 2020, 22: 100325.
- Sakhno, I., Sakhno, S. Numerical studies of floor heave mechanism and the effectiveness of grouting reinforcement of roadway in soft rock containing the mine water. *International Journal of Rock Mechanics and Mining Sciences*, 2023, 170: 105484.
- Schuler, H., Mayrhofer, C., Thoma, K. Spall experiments for the measurement of the tensile strength and fracture energy of concrete at high strain rates. *International Journal of Impact Engineering*, 2006, 32(10): 1635-1650.
- Shi, L., Zhou, H., Song, M., et al. Geomechanical model test for analysis of surrounding rock behaviours in composite strata. *Journal of Rock Mechanics and Geotechnical Engineering*, 2021, 13(4): 774-786.
- Tan, Y., Ma, Q., Zhao, Z., et al. Cooperative bearing behaviors of roadside support and surrounding rocks along gob-side. *Geomechanics and Engineering*, 2019, 18(4): 439-448.
- Wang, X., Cai, M. A method to estimate shear quality factor of hard rocks. *Pure and Applied Geophysics*, 2017, 174: 2689-2703.
- Wang, S., Hao, S., Chen, Y., et al. Numerical investigation of coal pillar failure under simultaneous static and dynamic loading. *International Journal of Rock Mechanics and Mining Sciences*, 2016, 84: 59-68.
- Wang, Y., Singh, S. C., Barton, P. J. Separation of P-and SV-wave fields from multi-component seismic data in the  $\tau - p$  domain. *Geophysical Journal International*, 2002, 151(2): 663-672.
- Wang, P., Zhang, N., Kan, J., et al. Instability mode and control technology of surrounding rock in composite roof coal roadway under multiple dynamic pressure disturbances. *Geofluids*, 2022, 2022: 8694325.
- Wen, X. Research and application of seismic random noise attenuation by improved Empirical Mode Decomposition method. Changchun City, Jilin University, 2022. (in Chinese)
- Wicaksana, Y., Jeong, H., Jeon, S. Numerical simulation of rock cutting process induced by a pick cutter considering dynamic properties of rock at intermediate strain rate. *Bulletin of Engineering Geology and the Environment*, 2021, 80(12): 9049-9069.
- Yan, L., Haider, A., Li, P., et al. A numerical study on the transverse seismic response of lined circular tunnels under obliquely incident asynchronous P and SV waves. *Tunneling and Underground Space Technology*, 2020, 97: 103235.
- Zang, C., Chen, Y., Chen, M., et al. Research on deformation characteristics and control technology of soft rock roadway under dynamic disturbance. *Shock and Vibration*, 2021, 2021: 6625233.
- Zhou, R., Cheng, H., Cai, H., et al. Dynamic characteristics and damage constitutive model of mudstone under impact loading. *Materials*, 2022, 15(3): 1128.
- Zuo, T., Zhao, Z., Wang, J., et al. Analysis of dynamic damage fractal and energy consumption characteristics of dolomite marble. *Shock and Vibration*, 2022, 2022: 9440222.